a protein complex, and additional subunits may be required for its activity and could be limiting in vivo. Indeed, immunoprecipitation of Ttll1p-GFP from overproducing *Tetrahymena* cells led to a recovery of polyglutamylase activity.

Ttll6Ap is a much larger protein (116 kD) than TTLL1 (49 kD) and Ttll1p (42 kD), and it may contain all properties required for autonomous polyglutamylase activity. The four noncatalytic subunits identified in the neuronal TTLL1 complex may be involved in tubulin substrate recognition, regulation of enzymatic activity, or subcellular localization, as has been suggested for PGs1 (*11*). It is likely that Ttll1p is also in a complex, as is the murine homolog. Except for PGs4, we could not identify homologs of the other subunits of the neural complex (PGs1, PGs2, PGs5) outside of vertebrates, including *Tetrahymena*; therefore, variations in the composition of noncatalytic subunits likely occur across phyla. The unusually large number of TTLL genes in *Tetrahymena* and the lack of a detectable loss-of-function phenotype for *TTLL1* suggest functional redundancy. In contrast, a mutation in the PGs1 component of the murine TTLL1 complex led to defective sperm axonemes and changes in animal behavior (*14*). In *Caenorhabditis elegans*, RNA interference (RNAi) depletion of *C55A6.2* (a TTLL5 type) causes embryonic lethality and sterility (*25*). Depletion of TTLL1 mRNA in PC12-E2 cells inhibited neurite outgrowth, suggesting an essential function in neurogenesis (*22*).

The phylogenetic association of TTLL1, TTLL9, TTLL4, TTLL6, TTLL5, and TTLL15 protein types (86% bootstrap value; Fig. 4) suggests that these protein types are all involved in glutamylation of tubulin or possibly of other proteins such as NAPs (*4*). Other members of the TTLL family may catalyze different types of posttranslational addition of an amino acid, such as polyglycylation (*26*).

References and Notes

1. B. Eddé *et al.*, *Science* **247**, 83 (1990).
2. M. Rüdiger, U. Plessman, K. D. Kloppel, J. Wehland, K. Weber, *FEBS Lett.* **308**, 101 (1992).
3. V. Redeker, R. Melki, D. Prome, J. P. Le Caer, J. Rossier, *FEBS Lett.* **313**, 185 (1992).
4. C. Regnard *et al.*, *J. Biol. Chem.* **275**, 15969 (2000).
5. C. Bonnet *et al.*, *J. Biol. Chem.* **276**, 12839 (2001).
6. Y. Bobinnec *et al.*, *J. Cell Biol.* **143**, 1575 (1998).
7. C. Gagnon *et al.*, *J. Cell Sci.* **109**, 1545 (1996).
8. K. Million *et al.*, *J. Cell Sci.* **112**, 4357 (1999).
9. Y. Bobinnec *et al.*, *Cell Motil. Cytoskeleton* **39**, 223 (1998).
10. C. Regnard, E. Desbruyères, P. Denoulet, B. Eddé, *J. Cell Sci.* **112**, 4281 (1999).
11. C. Regnard *et al.*, *J. Cell Sci.* **116**, 4181 (2003).
12. C. Regnard, S. Audebert, E. Desbruyères, P. Denoulet, B. Eddé, *Biochemistry* **37**, 8395 (1998).
13. The three more acidic spots of p32 contain phosphorylated peptides 277 to 284 (Arg-Pro-Ser-Val-Pro-Met-Ala-Arg) (Fig. 1A, spots 5 to 7). Phosphorylation site prediction (ExPASy Proteomics Server, www.expasy.org) indicates that Ser^{279} can be phosphorylated by cAMP- or cGMP-dependent protein kinases.
14. P. K. Campbell *et al.*, *Genetics* **162**, 307 (2002).
15. V. Trichet, M. Ruault, G. Roizes, A. De Sario, *Gene* **257**, 109 (2000).
16. K. Ersfeld *et al.*, *J. Cell Biol.* **120**, 725 (1993).
17. M. Y. Galperin, E. V. Koonin, *Protein Sci.* **6**, 2639 (1997).
18. J. Gaertig, *J. Eukaryot. Microbiol.* **47**, 185 (2000).
19. K. Rogowski, J. Gaertig, unpublished data.
20. The Institute for Genomic Research, *Tetrahymena thermophila* Sequence BLAST Search (http://tigrblast.tigr.org/er-blast/index.cgi?project=ttg).
21. Y. Shang *et al.*, *Proc. Natl. Acad. Sci. U.S.A.* **99**, 3734 (2002).
22. C. Janke *et al.*, data not shown.
23. S. F. Preston, G. G. Deanin, R. K. Hanson, M. W. Gordon, *J. Mol. Evol.* **13**, 233 (1979).
24. D. Raybin, M. Flavin, *J. Cell Biol.* **73**, 492 (1977).
25. I. Maeda, Y. Kohara, M. Yamamoto, A. Sugimoto, *Curr. Biol.* **11**, 171 (2001).
26. V. Redeker *et al.*, *Science* **266**, 1688 (1994).
27. T. Hara, H. Kato, Y. Katsube, J. Oda, *Biochemistry* **35**, 11967 (1996).

28. Supported by Association de la Recherche contre le Cancer award ARC 5859 (B.E.), Fondation pour la Recherche Médicale award INE20021108027/1 (C.J.), NSF award MBC-0235826 (J.G.), and EMBO long-term fellowship ALTF 387-2001 (C.J.). Preliminary sequence data for *Tetrahymena thermophila* were obtained from The Institute for Genomic Research. We thank E. Desbruyères, G. Herrada-Aldrian, J. M. Donnay, A. Bernet, and G. Rabeharivelo for technical assistance; P. Chaussepied, J. Frankel, M. Gorovsky, E. Kipreos, and M. Fechheimer for helpful comments; R. Melki for antibody to Arp1; S. Dettwiler and W. Keller for antibody to CF Im25; M. Gorovsky for antibodies polyG and polyE; K. Weber and S. Westermann for mAb ID5; and J. Frankel for mAb 12G10. Molecular interaction data have been deposited in the Biomolecular Interaction Network Database with accession code 295280.

Supporting Online Material
www.sciencemag.org/cgi/content/full/1113010/DC1
Materials and Methods
Figs. S1 to S5
Table S1
References

31 March 2005; accepted 28 April 2005
Published online 12 May 2005;
10.1126/science.1113010
Include this information when citing this paper.

REPORTS

Quantum Interference Device Made by DNA Templating of Superconducting Nanowires

David S. Hopkins, David Pekker, Paul M. Goldbart, Alexey Bezryadin*

The application of single molecules as templates for nanodevices is a promising direction for nanotechnology. We used a pair of suspended DNA molecules as templates for superconducting two-nanowire devices. Because the resulting wires are very thin, comparable to the DNA molecules themselves, they are susceptible to thermal fluctuations typical for one-dimensional superconductors and exhibit a nonzero resistance over a broad temperature range. We observed resistance oscillations in these two-nanowire structures that are different from the usual Little-Parks oscillations. Here, we provide a quantitative explanation for the observed quantum interference phenomenon, which takes into account strong phase gradients created in the leads by the applied magnetic field.

DNA has recently been considered as a "backbone" for the fabrication of information-processing devices, chemical and biological sensors, and molecular transistors at the nanometer-size scale (*1*, *2*). By taking advantage of DNA self-assembly possibilities (*3*), one can envision using single DNA and self-assembled DNA constructs as scaffolds for precise nanometer-scale positioning of other molecules and nanoscale objects. Recently, electronic devices with features that have molecular-scale dimensions have been assembled on such molecular-scale scaffolds (*4*). One of the simplest practical realizations of this approach lies in the metallization of DNA molecules (*5*). Previously, a wet-chemistry approach was used to metallize DNA (*5*–*8*), which tends to yield rather granular wires that become highly resistive at low temperatures.

We used a physical method of metallization [analogous to (*9*)] that involves sputter deposition of metallic films over suspended DNA molecules to fabricate wires as thin as 3 to 4 molecular diameters (as thin as 5 to 15 nm). Our nanowires are homogeneous, make seamless contacts with the leads, and become superconducting at low temperatures. We

Department of Physics and Frederick Seitz Materials Research Laboratory, University of Illinois at Urbana-Champaign, Urbana, IL 61801, USA.

*To whom correspondence should be addressed. E-mail: bezryadi@uiuc.edu

fabricated structures with pairs of such DNA-templated nanowires (Fig. 1) (*10*) to study quantum interference effects and the effect of thermal fluctuations at the nanoscale. Well-known examples of quantum interference include critical-current oscillations in conventional superconducting quantum interference devices (SQUIDs) (*11*, *12*) and Little-Parks resistance oscillations in thin-walled cylinders (*13*). In these examples, the periods of the oscillations are controlled by the superconducting flux quantum $\Phi_0(\equiv h/2e)$ where h is Planck's constant and $-e$ is the electronic charge, divided by the geometrical area enclosing the magnetic field. Our measurements on two-nanowire devices show a strong discrepancy with the usual behavior, and we provide a quantitative theoretical explanation for the observed period and amplitude of the oscillations.

Transport measurements at temperatures as low as 0.3 K at various magnetic fields (*10*) reveal a resistive transition, associated with the development of superconducting phase coherence throughout the nanowires, occurring over a broad temperature range in the absence of a magnetic field (Fig. 2A). This transition is found to broaden and narrow periodically with magnetic field. Consequently, at any temperature in the transition region, we see highly pronounced and very regular oscillations of the resistance with magnetic field (Fig. 2B). For higher temperatures in this region, the oscillation appears cosinusoidal, with a maximum in the amplitude at some intermediate temperature. For each sample, the observed period does not show any temperature or field dependence.

What distinguishes our resistance oscillations from those found, for example, by Little and Parks? First, the most notable aspect of these oscillations is the value of the measured period (456 μT in Fig. 2B), which is far shorter than one would estimate on the basis of the superconducting flux quantum divided by the area of the hole between the wires ($\Phi_0/2ab$ = 25 mT with dimensions a and b, defined in Fig. 1A, for sample 219-4 of Table 1). Thus, we see that the period of our oscillations is not controlled by the geometrical area defined by the nanowires and the edges of the leads. Instead, we find that in the low magnetic-field regime (when no vortices are present in the leads), the period is controlled by Φ_0 divided by a new quantity: the product of the lead width ($2l \sim$ 9 to 15 μm) and the interwire spacing ($2a \sim$ 0.3 to 4 μm). The reason for this is that the leads are mesoscopic—i.e., they are narrower than the perpendicular magnetic penetration depth ($\lambda_\perp \sim 70$ μm)—and therefore the magnetic field penetrates the leads with negligible attenuation. Second, because the resistance is caused by thermal phase fluctuations (i.e., phase slips) in very narrow wires, the oscillations are observable over a wide range of temperatures (~1 K). Third, the Little-Parks resistance is wholly ascribed to a rigid shift of the $R(T)$ curve with magnetic field as the critical temperature T_c oscillates. In contrast, in our system we find a much more substantial contribution to the resistance oscillations coming from the modulation of the barrier heights for phase slips.

Superconducting nanowires are unusual in that they never show zero resistance, although resistance does decrease exponentially upon cooling. As discussed by Little (*14*), Langer and Ambegaokar (LA) (*15*), and McCumber and Halperin (MH) (*16*), the origin of this resistive behavior lies in the occurrence of thermally activated slips of the phase of the Ginzburg-Landau (GL) order parameter $\psi(\vec{r})$. During a phase slip, a small normal segment appears on the nanowire for a short time, causing the loss of phase coherence between the leads. Resistance is then associated with a nonzero value of the average voltage, which matches the imbalance, due to the current, between forward and backward phase slips (*12*).

We developed an extension of LAMH theory that applies to devices containing two nanowires connected in parallel, including the effect of an applied magnetic field. The model accurately describes the period, magnitude, and temperature dependence of the observed magnetoresistance oscillations. The essential ingredients in our model are (i) leads, in which the applied magnetic field induces supercurrents and, hence, gradients in the phase of the order parameter and (ii) the two wires, whose behavior is controlled by the leads through the boundary conditions imposed by the leads on the phase of the order parameters in the wires. We assume that the wires have sufficiently small cross sections that the currents through them do not feed back on the order parameter in the leads.

In our model, thermally activated phase slips cause the superconducting order parameter to explore a discrete family of local minima of the free energy. These minima (and the saddle-point states connecting them) may be indexed by the net (i.e., forward minus reverse) number of phase slips that have occurred in each wire (n_1 and n_2) or, more usefully, by $n_s = \min(n_1, n_2)$ (i.e., the net number of phase slips that have passed through both wires) and $n_v = n_1 - n_2$ (i.e., the number of vortices accumulated in the loop, which is formed by the wires and the edges of the leads). Notably, two configurations with identical n_v but distinct n_s and n_s' have identical order parameters but differ in energy by $\Phi_0 I (n_s' - n_s)$, due to the work done by the current source supplying the current I.

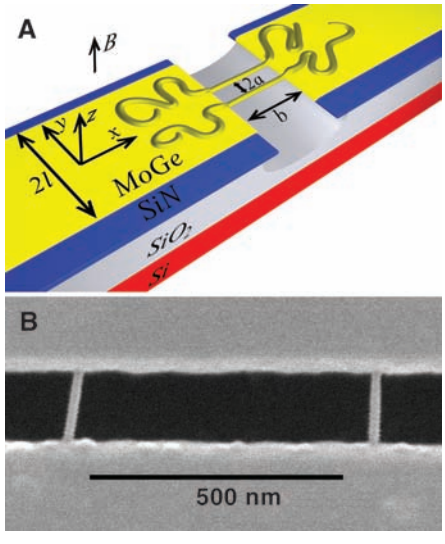

Fig. 1. (**A**) Schematic of the DNA-templated two-nanowire device. Two strands of DNA are stretched across a trench etched into SiN/SiO_2 on a Si chip (*6*). The molecules and the banks are coated with superconducting $Mo_{21}Ge_{79}$. The dimensions are indicated. (**B**) SEM micrograph of two metal-coated DNA molecules (sample 219-4).

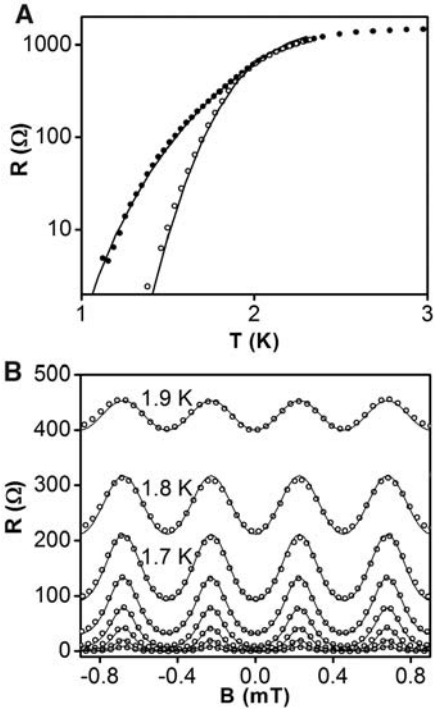

Fig. 2. (**A**) Resistance versus temperature measurements (sample 219-4) in zero magnetic field (open circles) and at a magnetic field of 228 μT (solid circles) corresponding to a maximum change in magnetoresistance. The lines are theoretical fits, based on the short-wire limit of our theory, with the following fitting parameters: J_{c1} = 639 nA, J_{c2} = 330 nA, T_{c1} = 2.98 K, and T_{c2} = 2.00 K, with corresponding coherence lengths $\xi_1(0)$ = 23 nm and $\xi_2(0)$ = 30 nm. (**B**) Resistance versus magnetic field measurements (sample 219-4) at temperatures from 1.2 to 1.9 K in 0.1 K increments. The lines are theoretical fits using the same fitting parameters as in (A) with the period set to 456 μT. Resistance is measured in ohms.

Table 1. A summary of the geometries (obtained from SEM), the theoretical predictions for the period of the magnetoresistance oscillations, and the measured periods for all of the two-wire devices. The geometry of 930-1 was changed by milling with a focused ion beam, and the magnetoresistance period was remeasured. Wire sep., wire separation; Th. per., theoretical period; Ex. per., experimental period, diff., difference.

Sample	Wire length b (nm)	Wire sep. $2a$ (nm)	Lead width $2l$ (nm)	Th. per. ΔB (μT)	Ex. per. (μT)	% diff.
205-4	121	265	11270	929	947	1.9
219-4	137	595	12060	389	456	14.8
930-1	141	2450	14480	78.4	77.5	–1.2
930-1 (FIB-narrowed leads)	141	2450	8930	127	128	0.9
205-2	134	4050	14520	47.4	48.9	3.0

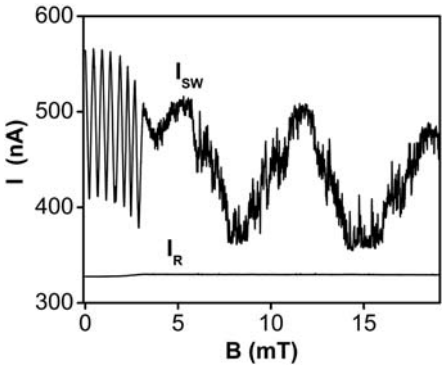

Fig. 3. Critical switching (I_{SW}) and retrapping (I_R) currents plotted versus magnetic field, measured at T = 285 mK (sample 219-4).

Due to the screening currents in the left lead (Fig. 1A), induced by the applied perpendicular magnetic field B (and independent of the wires), there is a field-dependent phase $\delta_{1\to 2,L}(B) = \int_1^2 d\vec{r} \cdot \vec{\nabla}\varphi(B)$, where $\varphi(B)$ is the field-dependent phase of the order parameter, accumulated in passing from the point at which wire 1 (the back one) contacts the left (L) lead to the point at which wire 2 (the front one) contacts the left lead. Similarly, the field creates a phase accumulation $\delta_{1\to 2,R}(B)$ between the contact points in the right (R) lead. Because leads are geometrically identical, the phase accumulations in them differ in sign only, $\delta_{1\to 2,L}(B) = -\delta_{1\to 2,R}(B)$. We define $\delta(B) = \delta_{1\to 2,L}(B)$. In determining the local free-energy minima, we solve the GL equation for the wires for each vortex number n_v, imposing the single-valuedness condition on the order parameter, $\theta_{1,R\to L} - \theta_{2,R\to L} + 2\delta(B) = 2\pi n_v$. Here, $\theta_{1,R\to L} = \int_R^L d\vec{r} \cdot \vec{\nabla}\varphi$ is the phase accumulated along wire 1 in passing from the right to the left lead; $\theta_{2,R\to L}$ is similarly defined for wire 2. Because we can neglect the direct effect of the magnetic field on the wires, $\delta(B)$ is the only field-dependent parameter that affects the wires. The magnetic field increases $\delta(B)$ and imposes additional phase gradients in the wires, which, according to LAMH theory, decrease the barriers for phase slips and, hence, increase the resistance. The period of the observed oscillations is derived from the fact that whenever the magnetic field is such that $2\delta(B) = 2\pi m$ (where m is an integer, and the factor of 2 reflects the presence of two leads), the family of free-energy minima (all of which are statistically populated according to their energies) of the two-wire system is identical to the $B = 0$ case. The identity is established by redefining $n_v \to n_v - m$. Thus, the resistance of the device returns to the zero-field value each time the phase accumulation in the leads satisfies $\delta = \pi m$.

Next, we describe how $\delta = \delta(B)$ is calculated. Consider an infinitely long, thin-film, superconducting strip of width $2l$, much narrower than the perpendicular penetration depth and subject to a uniform, perpendicular magnetic field $B\hat{z}$, sufficiently weak that no vortices are present in the strip. The vector potential $\vec{A} = By\hat{x}$ is always in the plane of the strip with $\vec{A} = 0$ along the middle of the strip. Thus, for the infinite strip, we have the London gauge (*12*) and the two-dimensional current density is $\vec{J}(x,y) = -t_f\vec{A}(x,y)/\mu_0\lambda^2 = -(t_f By/\mu_0\lambda^2)\hat{x}$, where t_f is the film thickness and λ is the magnetic penetration depth. Then, $\vec{J}$ has magnitude $t_f Bl/\mu_0\lambda^2$ at the strip edges. In our experiment, the lengths of the two leads are much greater than their widths. Thus, the above estimate for the current density near the long edges continues to hold. By continuity, this edge current must sweep around at the short edges of the leads and, in so doing, must flow in the $\hat{y}$ direction as it passes the connection points of the wires. Owing to the finite length of the leads, our choice of gauge is not London type, given that the vector potential is perpendicular to the short edges of the leads. Thus, the supercurrent along the short edges is determined by the gradient of the phase, by $\vec{J}(x,y) = (t_{film}\Phi_0/2\pi\mu_0\lambda^2)(\nabla_y\varphi)\,\hat{y}$, which means that $\nabla_y\varphi \approx (2\pi/\Phi_0)Bl$. Correspondingly, the phase drop between the ends of the wires is approximately given by $\delta(B) = 2\pi(2alB/\Phi_0)$. It follows that the period of the resistance oscillations, ΔB, is given by $\Phi_0/4al$. A more precise analysis (valid for the case $a << l$) [supporting online material (SOM) text] yields $\Delta B = (\pi^2/8G)(\Phi_0/4al)$, where $G = 0.916\ldots$ is the Catalan number.

To test our prediction for the period, we measured five different samples (Table 1) and extracted the periods from the corresponding $R(B)$ curves. Table 1 shows the excellent agreement between the theoretically calculated and measured periods. Only one sample (219-4) showed a 15% deviation from the theoretical prediction. A scanning electron microscopy (SEM) inspection of the leads of this sample revealed that the lead shape was not precisely rectangular (fig. S1), in contrast with all other samples. Thus the current flow near the ends of the wires in 219-4 was distorted, explaining the observed deviation. A more stringent test of the formula for the period was obtained by narrowing the leads of one of the samples (930-1) with the use of a focused ion beam (FIB) milling and remeasuring the period and the lead width: The new period was larger and remained in excellent agreement with the new calculated value (Table 1). One can also account for an additional Aharonov-Bohm phase shift associated with the vector-potential integrated around the loop formed by the wires. In our geometry, this effect accounts for a ~1% correction to the calculated period, which is slightly below the accuracy of our measurements and was neglected (SOM text).

We now consider the question of the magnitude of the resistance oscillations. In our theory, the phase slip rate Γ between various local free-energy minima takes into account the response of one wire to any phase slip occurring in the other wire, and is determined by Arrhenius law $\Gamma = \Omega\exp[-\Delta F/k_B T]$, where Ω is the attempt frequency and k_B is the Boltzmann constant. The free-energy barrier ΔF for a phase slip depends on the initial and final configurations, each of which is defined by a pair of integers n_v and n_s. The zero-bias resistance is $R = V/I$, where the current I is small and fixed and the voltage is given by $V = (\hbar/2e)\dot{\varphi}$, where $\hbar$ is $h/2\pi$. The net phase slip velocity $\dot{\varphi} = 2\pi\dot{n}_s$ is determined by the net number of phase slips that pass through both wires per unit time, which in turn depends on Γ. For example, in the short-wire limit ($b < 4\xi$, where b is the wire length and ξ is the superconducting coherence length), we always have $n_v = 0$, and the resistance is $R = (\pi\hbar^2\Omega/2e^2\,k_B T)\,\exp[-\Delta F/k_B T]$. In the same limit, the barrier height is $\Delta F = (\hbar/e)$

$$\sqrt{(j_{c1}+j_{c2})^2\cos^2\delta(B) + (j_{c1}-j_{c2})^2\sin^2\delta(B)}.$$

Here, j_{c1} and j_{c2} are the critical currents for the wires, given by $j_c = [113\ \mu A][bT_c/R_N\xi(0)][1 - (T/T_c)]^{3/2}$, where T_c is the critical temperature of the corresponding wire, R_N is its normal state resistance, and ξ is its coherence length (*17*). The fit of the predictions of our model to the experimental data is shown as the solid curves in Fig. 2A (SOM text).

So far, we have concentrated on phenomena at magnetic fields below roughly 3 mT,

and for such fields we observed short-period, nonhysteretic resistance oscillations. Whenever fields larger than this scale have been applied, the magnetoresistance behavior becomes hysteretic, even if the field is swept back to the sub–3 mT regime. The most natural explanation for this transition follows from Likharev's threshold-field theory, according to which vortices start to enter the thin film leads at fields of this magnitude (*18–21*). Once present, some vortices remain in the leads and contribute the phase shifts experienced by the wires, and therefore can influence the measured resistance. To reduce the noise caused by the thermal motion of vortices, we measured (*10*) the switching and retrapping critical currents (instead of resistance) versus the magnetic field at $T = 0.3$ K (Fig. 3). It is clear that only the switching current shows oscillations, whereas the retrapping current is field independent. No detailed explanation for this interesting phenomenon is known to us at this point. Notably, the period of the switching current oscillation in the low-field regime coincides with that of the magnetoresistance (fig. S2). Two types of oscillatory behavior are observed (Fig. 3). The short-period oscillation corresponds to the fields at which no vortices are present and the large-period oscillation occurs when vortices have entered the leads. The large period changes with magnetic field and can be estimated as $\Delta B_{large} \sim \Phi_0/2a(d + b)$, where d is the distance between the vortices.

We report a new class of metallic devices based on DNA molecules. Such an approach is promising, due to the self-assembly properties of DNA. As the resistance of the devices is controlled by the spatial profile of the superconducting phase within the leads, there is the potential for applications. These include local magnetometry (as is widely done with conventional SQUIDs) and the imaging of phase profiles created by supercurrents—in essence a superconducting phase gradiometer. Applications are not limited to a narrow range of temperatures; the ultranarrow widths of the wires ensure that the resistive transition occurs over a broad range of temperatures.

References and Notes

1. E. Braun, K. Keren, *Adv. Phys.* **53**, 441 (2004).
2. H. Watanabe, C. Manabe, T. Shigematsu, K. Shimotani, M. Shimizu, *Appl. Phys. Lett.* **79**, 2462 (2001).
3. N. C. Seeman, *Angew. Chem. Int. Ed.* **37**, 3220 (1998).
4. H. Yan, S. H. Park, G. Finkelstein, J. H. Reif, T. H. LaBean, *Science* **301**, 1882 (2003).
5. E. Braun, Y. Eichen, U. Sivan, G. Ben-Yoseph, *Nature* **391**, 775 (1998).
6. J. Richter, M. Mertig, W. Pompe, I. Monch, H. K. Schakert, *Appl. Phys. Lett.* **78**, 536 (2001).
7. J. Richter, M. Mertig, W. Pompe, H. Vinzelberg, *Appl. Phys. A* **74**, 725 (2002).
8. M. Mertig, L. C. Ciacchi, R. Seidel, W. Pompe, *Nano Lett.* **2**, 841 (2002).
9. A. Bezryadin, C. N. Lau, M. Tinkham, *Nature* **404**, 971 (2000).
10. Materials and Methods are available as supporting material on *Science* Online.
11. R. C. Jaklevic, J. Lambe, A. H. Silver, J. E. Mercereau, *Phys. Rev. Lett.* **12**, 159 (1964).
12. M. Tinkham, *Introduction to Superconductivity* (McGraw-Hill, New York, ed. 2, 1996).
13. W. A. Little, R. D. Parks, *Phys. Rev. Lett.* **9**, 9 (1962).
14. W. A. Little, *Phys. Rev.* **156**, 396 (1967).
15. J. S. Langer, V. Ambegaokar, *Phys. Rev.* **164**, 498 (1967).
16. D. E. McCumber, B. I. Halperin, *Phys. Rev. B* **1**, 1054 (1970).
17. M. Tinkham, C. N. Lau, *Appl. Phys. Lett.* **80**, 2946 (2002).
18. K. K. Likharev, *Sov. Radiophys.* **14**, 722 (1973).
19. J. R. Clem, *Bull. Am. Phys. Soc.* **43**, 411 (1972).
20. G. M. Maksimova, *Phys. Solid State* **40**, 1610 (1998).
21. G. Stan, S. B. Field, J. M. Martinis, *Phys. Rev. Lett.* **92**, 097003 (2004).

22. Supported by NSF CAREER grant no. DMR 01-34770, the A. P. Sloan Foundation (D.S.H. and A.B.), and the U.S. Department of Energy, Division of Materials Sciences under award no. DEFG02-91ER45439, through the Frederick Seitz Materials Research Laboratory at the University of Illinois at Urbana-Champaign, and the Center for Microanalysis of Materials Department of Energy grant no. DEFG02-96ER45439.

Supporting Online Material

www.sciencemag.org/cgi/content/full/308/5729/1762/DC1
Materials and Methods
SOM Text
Figs. S1 to S5
References

22 February 2005; accepted 28 April 2005
10.1126/science.1111307

Spectral Signatures of Hydrated Proton Vibrations in Water Clusters

Jeffrey M. Headrick,[1] Eric G. Diken,[1] Richard S. Walters,[2] Nathan I. Hammer,[1] Richard A. Christie,[3] Jun Cui,[3] Evgeniy M. Myshakin,[3] Michael A. Duncan,[2]* Mark A. Johnson,[1]* Kenneth D. Jordan[3]*

The ease with which the pH of water is measured obscures the fact that there is presently no clear molecular description for the hydrated proton. The mid-infrared spectrum of bulk aqueous acid, for example, is too diffuse to establish the roles of the putative Eigen (H_3O^+) and Zundel ($H_5O_2^+$) ion cores. To expose the local environment of the excess charge, we report how the vibrational spectrum of protonated water clusters evolves in the size range from 2 to 11 water molecules. Signature bands indicating embedded Eigen or Zundel limiting forms are observed in all of the spectra with the exception of the three- and five-membered clusters. These unique species display bands appearing at intermediate energies, reflecting asymmetric solvation of the core ion. Taken together, the data reveal the pronounced spectral impact of subtle changes in the hydration environment.

Despite the ubiquity of aqueous acids in chemical and biological systems (*1–7*), a molecular-level description of the hydrated proton remains elusive (*8–14*). The suggestion in introductory chemistry texts that the dominant speciation occurs as "hydronium" [H_3O^+, also called the Eigen (*9*) core] is too simplistic; an alternative limiting form proposed by Zundel (*10*) $(H_2O\cdots H\cdots OH_2)^+$ has long been thought to play an essential role, and the broad infrared absorptions of the aqueous proton at 1250, 1760, and 3020 cm^{-1} have been assigned in the context of both the Eigen and Zundel species (*15–17*). Here, we characterize the hydrated proton using a bottom-up approach. Through recent advances in laser generation of infrared light in the 1000- to 4000-cm^{-1} range, we directly monitor the spectral evolution of the proton accommodation motif as water molecules are sequentially added to the hydronium ion, up to an 11-membered cluster.

Infrared spectra of bare $H^+ \cdot (H_2O)_n$ clusters in the OH stretching region (2800 to 3900 cm^{-1}, with inconsistent coverage below 2800 cm^{-1}) have already been reported, and the observed bands are mostly attributed to water molecules remote from the proton (*18–23*). Dangling water molecules attached to the exterior of a hydrogen-bonded network, for example, produce sharp bands arising from the symmetric (υ_s) and asymmetric (υ_a) stretches of the nonbonded OH groups. Theoretical analysis of these spectra indicated a Zundel motif for the two-, six-, seven-, and eight-membered clusters, but an embedded Eigen core for the three- to five-membered clusters (Fig. 1).

[1]Sterling Chemistry Laboratory, Yale University, Post Office Box 208107, New Haven, CT 06520, USA. [2]Department of Chemistry, University of Georgia, Athens, GA 30602, USA. [3]Department of Chemistry, University of Pittsburgh, Pittsburgh, PA 15260, USA.

*To whom correspondence should be addressed. E-mail: maduncan@uga.edu (M.A.D.), mark.johnson@yale.edu (M.A.J.), jordan@pitt.edu (K.D.J.)